Enhanced conduction and ferromagnetic order at (100)-type twin walls in $La_{0.7}Sr_{0.3}MnO_3$ thin films

Lluís Balcells,[1] Markos Paradinas,[1] Núria Baguès,[1,2] Neus Domingo,[2] Roberto Moreno,[2] Regina Galceran,[1] Michael Walls,[3] José Santiso,[2] Zorica Konstantinovic,[1] Alberto Pomar,[1] Marie-Jo Casanove,[4] Carmen Ocal,[1] Benjamín Martínez,[1] and Felip Sandiumenge[1,*]

[1]*Institut de Ciència de Materials de Barcelona, ICMAB-CSIC, Campus de la Universitat Autònoma de Barcelona, 08193 Bellaterra, Catalonia, Spain*

[2]*Centre for Nanoscience and Nanotechnology, CIN2 (CSIC-ICN), Campus de la Universitat Autònoma de Barcelona, 08193 Bellaterra, Catalonia, Spain*

[3]*Laboratoire de Physique des Solides, Bureau 242-2ème étage Est–Bâtiment 510–Rue André, Rivière, 91400 Orsay, France*

[4]*CNRS, CEMES, Universite de Toulouse UPS, 29 Rue J. Marvig, Toulouse 31055, France*

(Received 23 January 2015; revised manuscript received 27 May 2015; published 7 August 2015)

There is increasing evidence supporting the strong potential of twin walls in ferroic materials as distinct, spatially tunable, functional elements in future electronic devices. Here, we report an increase of about one order of magnitude in conductivity and more robust magnetic interactions at (100)-type twin walls in $La_{0.7}Sr_{0.3}MnO_3$ thin films. The nature and microscopic origin of such distinctive behavior is investigated by combining conductive, magnetic, and force modulation scanning force microscopies with transmission electron microscopy techniques. Our analyses indicate that the observed behavior is due to a severe compressive strained state within an $\sim$1 nm slab of material centered at the twin walls, promoting stronger Mn $3d-$O $2p$ orbital overlapping leading to a broader bandwidth and enhanced magnetic interactions.

DOI: 10.1103/PhysRevB.92.075111 PACS number(s): 77.80.Dj, 61.72.Mm, 73.63.−b, 75.47.Lx

I. INTRODUCTION

Domain walls in ferroic complex oxides are stirring up a lot of interest in nanoscience and nanotechnology owing to their intrinsically distinctive functional behavior relative to that exhibited by the host material [1,2]. Domain walls constitute a class of natural, spatially ordered, and tunable homointerfaces where, similar to complex oxide epitaxial heterointerfaces [3,4], symmetry breaking and stress promote emergent phenomena with new physics and functionalities at the nanoscale. Owing to the subtle interplay between charge, spin, orbital, and lattice degrees of freedom characterizing transition metal oxides [5], homointerface induced phenomena does not appear restricted to any particular type of ferroic order. Thus, for instance, ferroelectric domain walls in multiferroic materials with simultaneous ferrolectric and magnetic order, such as $BiFeO_3$, $YMnO_3$ or $TbMnO_3$, have been reported to exhibit variable levels of electrical conductance [6–8], or ferromagnetism [9], respectively, while an $\sim 10^9$ times increase in conductivity has been observed at strongly charged 90° head-to-head walls in the canonical ferroelectric $BaTiO_3$ [10]. On the other hand, twin walls (TWs) in nonferroelectric ferroelastics have been shown to exhibit ferroelectric polarization ($SrTiO_3$ [11]), two-dimensional superconductivity (WO_{3-x} [12]), or ferrielectricity ($CaTiO_3$ [13]), and computer simulations on undoped manganites (bulk insulating state with antiferromagnetic ordering) also predict an enhancement in conductance at TWs [14].

Ferroelastic TWs are defined to satisfy the compatibility between two orientations of the spontaneous strain on the contact plane which generally coincides with a prominent crystallographic plane [15], yet they are associated to large strain gradients perpendicular to it [16]. In strongly correlated electron oxides such distortions affect electrical and magnetic functionalities in an intricate way. As ABO_3 octahedral frameworks can deform by octahedral tilting (i.e., B-O-B bond angle distortion) and octahedral B-O bond length distortion simultaneously, the cornerstone in the interpretation of TW phenomena is the disentanglement of the strain state underpinning the coupling mechanism. To this end, various approaches based on aberration-corrected high resolution transmission electron microscopy have been reported [6,9,13,17,18]. In particular, experimental studies on the influence of chemical pressure in doped bulk materials [19,20] and theoretical investigations on thin films (see Ref. [21] and references therein) converge in identifying the competing effect of ⟨Mn-O-Mn⟩ bond angle and Mn-O bond length on the degree of orbital overlapping as the leading structural mechanism governing the bandwidth of these materials.

Among strongly correlated electron oxides, doped manganese perovskites exhibit a variety of phenomena, such as metal-insulator transition, half-metallic character, and cooperative orbital ordering [22]. However, despite their fascinating hetero-interfacial behavior (see, e.g., Ref. [23]), TWs in this materials remain unexplored. In this paper we focus on the TWs properties of the ferroelastic half-metallic $La_{0.7}Sr_{0.3}MnO_3$ (LSMO) room temperature ferromagnet, demonstrating that the electrical conductivity and ferromagnetic interactions at the surface of epitaxial thin films are substantially enhanced along the trace of (100) and (010) TWs perpendicular to the substrate. Using a combination of scanning probe and electron microscopies we are able to correlate this behavior with a strongly compressive state occurring at the TW which promotes stronger Mn $3d-$O $2p$ orbital overlapping leading to a broader bandwidth and enhanced magnetic interactions.

II. EXPERIMENT

LSMO thin films with thicknesses $t \sim 40-100$ nm were grown on (001)-oriented, TiO_2 terminated $SrTiO_3$ (STO)

*Corresponding author: felip@icmab.es

substrates by rf magnetron sputtering, as described in Ref. [24]. The topography of as-grown films consists of atomically flat terraces with a roughness below 0.3 Å bounded by unit cell (∼4 Å) height steps. Among the {100} and {110} TWs allowed in the $m3m \rightarrow \bar{3}m$ ferroelastic transition [15], only those with (100) and (010) orientations, perpendicular to the substrate, are present in these films [25,26]. The lateral twin size increases as $t^{1/2}$ [26]. The TDs remain fully in-plain strained by the substrate in the explored thickness range [25]. In-plane electrical resistivity and magnetization measurements of these samples are reported elsewhere [25].

Local electrical conductivity measurements were carried out using conducting scanning force microscopy (C-SFM) using a commercial head and software from Nanotec under an N_2 environment (RH ≈ 2%) to diminish any possible humidity effect. We used Si tips mounted on cantilevers with $k = 0.5$ N/m (Veeco) for friction force measurements (FFM) and commercial conductive CrPt coated Si tips mounted on cantilevers with $k = 40$ N/m (Budgetsensors). In at least one series of measurements the same tip was conserved for all experiments. To check tip-sample conditions, the adhesion force was systematically determined from force versus distance curves prior to and after each conductivity experiment. Current images were acquired in a noninvasive manner (the absence of sample indentation was always checked) by using the contact operation mode at the lowest possible applied load needed. The conducting tip (first electrode) was placed in direct contact with the sample, under controlled load, i.e., by using a normal force feedback, and the current was measured between tip and sample. Simultaneous topographic images $z(x,y)$ and current maps $I(x,y)$ were obtained over a given region at a fixed voltage. The current-voltage (I-V) characteristics of the contact were obtained as a function of the bias voltage applied between tip and sample at chosen specific single points on the surface (i.e., the lateral scan of the tip is disabled). In this mode, direct comparison between I-V characteristics at different locations on the $I(x,y)$ map is therefore possible. Both, forwards and backwards, current-voltage (I-V) characteristics of the contact where always measured starting from negative tip voltages. In our setup, the sample was always grounded and the voltage was applied to the tip. Because of the insulating character of the substrates used ($SrTiO_3$) the direct electric contact to ground is established through a metallic clamp (counterelectrode) firmly attached to the surface of the film at the sample border (millimeters apart from the tip-surface contact). An external I-V converter (Stanford Research Systems) was used to provide access to a wide range of compliance currents (1 pA to 1 mA). Whereas for topographic images the color code is the commonly used, bright for high and dark for low, for the current maps it depends on the voltage sign. Thus higher currents appear darker in C-SFM images taken at negative V_{tip} values, while brighter for positive V_{tip}.

The spatially resolved mechanical response of the surface of the films was analyzed by Force Modulation Microscopy (FMM, Asylum Research). FMM is a SFM-based mode where the tip in direct contact with the surface is forced to vibrate at a high frequency (contact resonance frequency typically of several 100's of KHz) in order to evaluate the mechanical response of the material [27–29]. Any variation in the contact resonance frequency is related to the local sample stiffness, i.e., a positive shift in frequency corresponds to stiffer mechanical properties. The topography was collected in contact mode and an ac voltage was applied to the piezoelectric actuator at the cantilever in order to induce this vibrational motion. The contact resonance frequency was tracked by a dual ac resonance tracking system. The topography of the films did not change during the measurement, meaning that they were performed in the elastic regime.

The spatially resolved magnetic behavior of the films was investigated by magnetic force microscopy (MFM). Images were taken with Nanosensors MFM tips, showing a nominal magnetic moment of 3×10^{-14} emu. Phase contrast images are obtained at different tip distances from the film surface (h), while adjusting the amplitude ratio (A_{MFM}/A_{sp}) of MFM imaging (A_{MFM}) *vs* topography imaging set point (A_{sp}). In this way, we obtained MFM images over different long range force areas and lateral spatial resolutions.

The local atomic and chemical structure of the TWs was studied by aberration-corrected high-resolution transmission electron microscopy techniques. Samples for TEM observation were prepared by conventional cutting-gluing-grinding procedures, followed by Ar milling down to perforation at a small incidence angle. Annular dark field images and electron energy-loss spectroscopy (EELS) spectrum-images (SI) of cross-section samples were acquired using a Nion Ultrastem 200 scanning transmission electron microscope (STEM) operating at 100 kV. The probe convergence angle was 35 mrad. The data shown here used a 50 mrad EELS collection angle (smaller angles did not significantly improve visible detail in the spectra, while greatly reducing signal). Data were denoised using principal components analysis (PCA) as provided in the Hyperspy suite [30]. To avoid the possibility of any small shift or signal shape change being lost through an excessive noise removal, the first three components appearing to contain only noise were left in the PCA reconstruction (i.e., three more components than would normally be retained in this analysis). The Mn edges in the spectra were then modeled also using Hyperspy over the energy-loss range 600−680 eV. The components in the model were an AE^{-r} type power law background, two Gaussian peaks centered on the L_2 and L_3 peak energies and continuum L_2 and L_3 edges as calculated via the Hartee-Slater method [31]. Atomic resolution phase contrast images were obtained in planar view orientation using a Hitachi HF3300 electron microscope working at 300 kV and equipped with a CFEG and an imaging aberration corrector CEOS aplanator.

III. RESULTS AND DISCUSSION

Figure 1(a) shows a typical orientation-contrast scanning electron micrograph (OC-SEM) image of the film used for nanoscale conductivity measurements, which clearly indicates a long range ordered pattern of TDs in the films. The different contrast levels reflect the various degrees of misorientation between different domains; see Ref. [26]. As shown in Fig. 1(b), the sample surface topography consists of flat terraces separated by unit cell height steps (see inset). In spite of the extremely flat surface morphology, the simultaneously acquired current map shown in Fig. 1(c) reveals a considerable

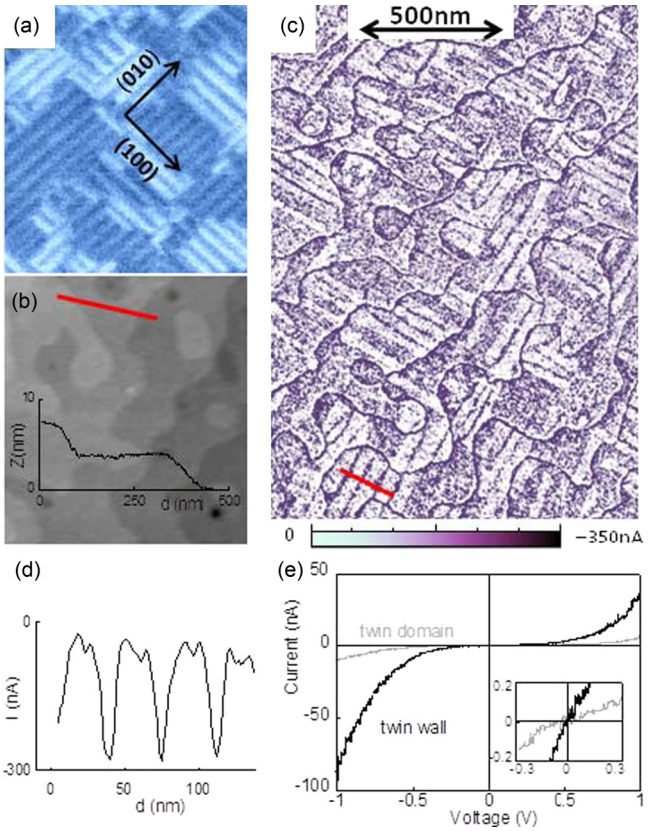

FIG. 1. (Color online) (a) OC-SEM image exhibiting the twin pattern, (b) SFM topographic image (profile along the red line shown as inset), and (c) current map acquired at $V = -1.4$ V, of a 40 nm thick LSMO film. Note that negative (dark) current values are measured for $V_{tip} < 0$. (a), (b), and (c) are presented with the same scale as indicated in (c). In (c), enhanced current running along the [100] and [010] directions corresponds to the TW locations. (d) Averaged current profile along the red line in (c). (e) I-V characteristics obtained at the TWs (black) and on the TD (gray). Each I-V corresponds to the average of five different measurements on the same position. In spite of the low current detected at low voltages both I-V curves present a linear behavior around $V = 0$] . Inset is a zoom at the linear regime.

intensity along lines running along (010) and (100) directions which are superimposed to a quite uniform current background [Figs. 1(c) and 1(d)]. The separation between conducting lines coincides with the lateral size of the TDs shown in Fig. 1(a) and forms domains of perpendicular orientations that perfectly mimic the twin pattern. Thus we correlate the position of the conducting lines with the position of TWs. As can be clearly seen, the meandering lines in current correspond to the step ledges and are due to extended tip-surface contact at them and therefore are not at the focus of the present study. However, as C-SFM measurements can be affected by local variations of the elastic response of the film surface leading to variations in tip-surface contact area, we probed the local mechanical response of the films by FMM. A clear positive shift of the contact resonance frequency was detected along the TWs, indicating that they are harder than the TDs (see Supplemental Material [32]). This observation rules out any contribution of surface elasticity to the observed enhancement

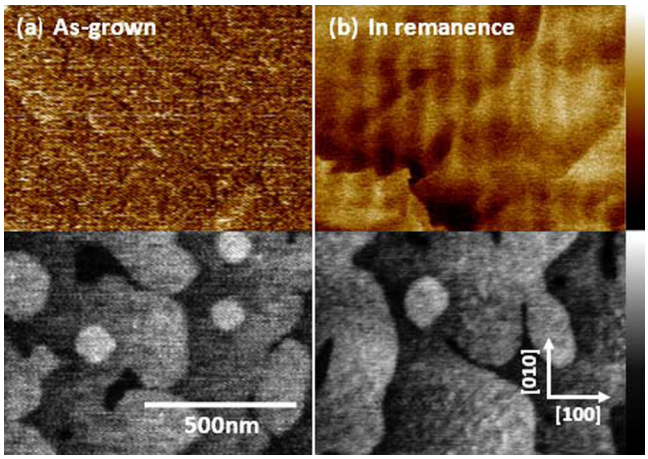

FIG. 2. (Color online) MFM images of an as-grown 100 nm thick LSMO film (a) and in the remanent state (b). Bottom images show the corresponding topographic images. In (b) the TWs appear brighter indicating a stronger tip-sample interaction. Color scale bars correspond to a full range of 2.5°] and 1.2 nm for MFM and topographic images, respectively.

in conductivity. Characteristic I-V curves obtained from one TW (black line) and an adjacent TD (gray line) are shown in Fig. 1(e). The voltage range was limited to ± 1.4 V to minimize undesired structural or chemical perturbations derived from the resistive switching effect observed in LSMO films [33]. The I-V response is linear at low voltages [see inset in Fig. 1(e)] as expected for tunneling conducting systems.

Similar to C-SFM, MFM images also bring out the presence of an ordered linear pattern matching the underlying arrangement of TWs, superimposed to an homogeneous darker background, as shown in Fig. 2. An analysis of the MFM contrast as a function of the tip-surface distance, h, is presented in Fig. 3. Figure 3(a) is a topographic image of the area analyzed in (b) through (d). Note that, as the tip-surface distance, h, is reduced from (b) to (d), the concomitant reduction in oscillation amplitude to avoid the short range topography interactions noticeably improves the lateral resolution of the images but deteriorates the signal to noise ratio. For higher distances, h, the tip magnetic moment mainly interacts with the stray fields of long-range ferromagnetically ordered magnetic moments present in the bulk of the sample, resulting in the low magnetic phase contrast over blurry areas as observed in Fig. 3(b). Superimposed to this interaction background, we can observe a series of lines running parallel to the [100] and [010] directions, that we attribute to the signal coming out from the TWs. At the working tip-sample distances shown in (b) and (c), the tip stray magnetic field is too weak to perturb the intrinsic magnetic order at the TWs. When the tip-surface distance is further reduced the TWs appear brighter than the TDs owing to a stronger attractive tip-sample interaction; at these distances, the tip stray magnetic fields are strong enough to overcome the coercive magnetic field of the TW and align the magnetic moments during the scan. From this analysis, the magnetic configuration of the films can be described as composed by two ferromagnetic materials, one corresponding to the TDs and a second one with larger ferromagnetic moment corresponding to the TWs.

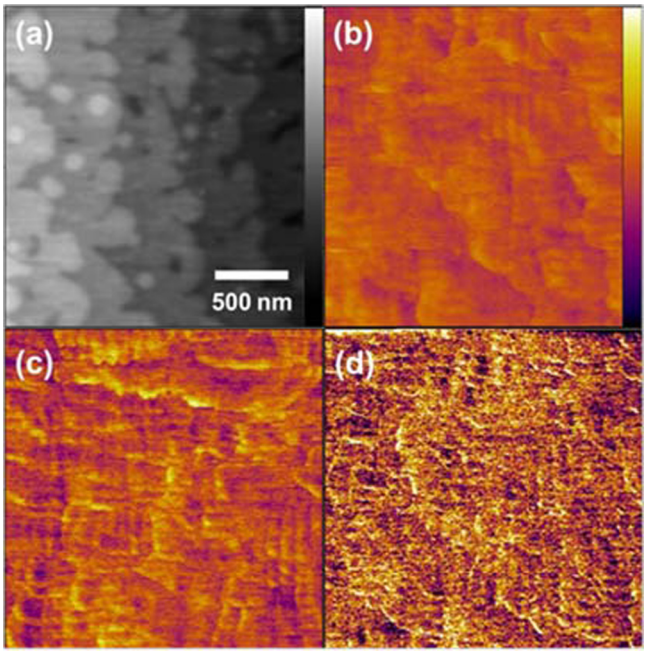

FIG. 3. (Color online) (a) Topography image over an area of 2 mm × 2 mm of the surface of a LSMO thin film. The color scale bar corresponds to a full range of 3 nm. (b) to (d) show the MFM phase contrast over the same area as in (a) under different conditions: (d) $h = 15$ nm and $A_{MFM}/A_{sp} = 0.9$, (c) $h = -11$ nm and $A_{MFM}/A_{sp} = 0.5$, and (d) $h = -22$ nm and $A_{MFM}/A_{sp} = 0.12$. The color scale bar for all MFM images is shown in (d) and corresponds to a full range scale of 2.5°. In (b) and (c) the tip coercive field is smaller than the coercive field of the TWs, which accordingly appear darker than the TDs. In (d) the tip coercive field becomes larger than the coercive of the TWs, causing a contrast reversal (TWs appear brighter than the TDs).

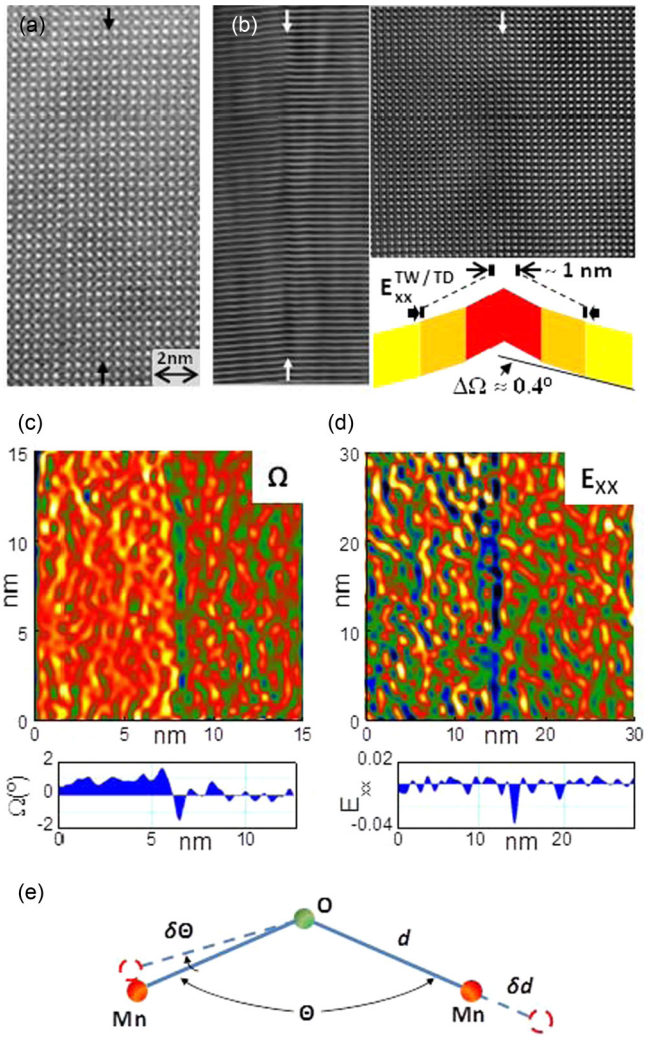

FIG. 4. (Color online) (a) Cross section HAADF image of a (100)-TW (indicated with vertical arrows) viewed along the [010] axis, of a 40 nm thick LSMO film. The position of the TW is only recognized by the tilt of the (001) planes by twin angle Ω. The contrast of atomic columns (proportional to their atomic number, Z) is not altered at the TW. (b) Right panel: planar view HRTEM image of a (100)-TW (indicated with vertical arrows) viewed along the [001] axis, of a 40 nm thick film. Left panel: same image but laterally compressed to emphasize the increase of Ω in the TW. Inset is a schematic drawing illustrating the distortion of the structure in the TW according to the GPA analysis presented below. (c) and (d) show the corresponding Ω and $E_{xx}^{TW/TD}$ maps, along with their averaged profiles, as obtained by GPA analysis. $E_{xx}^{TW/TD}$ is the strain component perpendicular to the TW, relative to the TD. (e) Distortion mechanisms of the octahedral framework: octahedral tilting distorts the ⟨Mn-O-Mn⟩ bond angle by $\delta\Theta$ and distortion of the MnO_6 octahedra results in the elastic stretching or compression (δd) of the Mn-O bond.

In order to understand the microscopic origin of the distinctive behavior of the TWs, we investigated their local structure and chemistry by combining different transmission electron microscopy techniques. Figure 4(a) is a cross section high-resolution high-angle annular dark-field (HAADF) image obtained around a TW. This is an incoherent image [34]; the influence of strains is negligible and the brightness of each atomic column is proportional to the atomic number, Z. Therefore, brighter and bigger dots correspond to the La/Sr sublattice, while columns of alternating Mn and O atoms are hardly visible. Careful inspection of the image does not reveal any distinctive feature associated to the position of the twin-plane separating the two adjacent TDs. Hence we conclude that cationic order is not significantly altered at the TW. Moreover, analysis of EEL spectra corresponding to the Mn-$L_{3/2}$ edges acquired within selected regions containing the TW and away from it did not reveal any signature of variations in the oxidation state of the Mn cations (see Supplemental Material [32]).

The strain state of the TW has been investigated by HRTEM. Since we are interested in the strain distribution along the trace of the TWs on the surface of the films, observations were performed in planar-view configuration; see Fig. 4(b). As in the HAADF image, direct inspection of the image shown in the right panel, only allows to recognize the TW through the tilt of the (001) or (100) planes, respectively, which corresponds to the twin angle, $\Omega = 2(\alpha_{pc} - 90°) \sim 0.8°$, where α_{pc} is the *pseudo*cubic interaxial angle. However, the laterally compressed image depicted in the left panel clearly reveals an increase of Ω seen as a cusp along the trace of the (100) planes. This effect is quantified in the Ω map shown in Fig. 4(c), computed from geometrical

phase analysis (GPA) [35]. This map clearly features a discontinuous ridge corresponding to an increase in Ω up to ∼1.5° within an ∼1 nm thick region centered at the TW. The corresponding map of the strain component perpendicular to the TW, also reveals an ∼1 nm thick region centered at the TW [see Fig. 4(d)] submitted to a severe compressive strain relative to the TD of $E_{xx}^{\mathrm{TW/TD}} = -3.5\%$, otherwise consistent with the increased hardness observed by FMM. The strain state of the TW deduced from this analysis is schematically depicted in Fig. 4(b); its consequences on the distortion of the octahedral framework are illustrated in Fig. 4(e). The twinned film thus can be viewed as a self-organized nanostructure consisting of 1 nm thick sheets of strongly compressed LSMO embedded in matrix of tensilely strained LSMO. In our GPA analysis $E_{xx}^{\mathrm{TW/TD}}$ is defined relative to the TD, which is fully in-plane strained by the STO substrate [25] (misfit $\delta \sim 0.6$); therefore, the effective compression relative to the bulk LSMO phase is of $\sim -2.9\%$.

The distortion of the octahedral framework building ABO_3 perovskites is conveniently described by a combination of rigid BO_6 octahedral rotations about the *pseudo*cubic unit cell axes, α (or equivalently ⟨Mn-O-Mn⟩ bond angle distortions, $\delta\Theta$) and elastic stretching/compression of the B-O bonds, δd, as shown in Fig. 4(e). In order to disentangle the strain state of the TW, here we take advantage of the link between Ω and the rigid octahedral tilts about the *pseudo*cubic unit cell axes, α, as derived from geometrical formalisms reported for rhombohedral perovskites [36]:

$$\alpha = \sin^{-1}\sqrt{3\,\cos\alpha_{\mathrm{pc}}/\left(1-2\,\cos\alpha_{\mathrm{pc}}\right)}/\sqrt[3]{3}, \qquad (1)$$

where $\alpha_{\mathrm{pc}} = (\Omega+\pi)/2$. The octahedral tilt inside the TW derived from this approximation is thus $\alpha_{\mathrm{TW}} = 7.55°$, larger than the bulk value, $\alpha = 5.2°$ (as calculated from ⟨Mn-O-Mn⟩ = 165.24° [37]). Using Eq. (1), the amount of strain accommodated by rigid octahedral tilts is only $\Delta a/a_{\mathrm{TD}} = \cos^2\Delta\alpha - 1 = -0.0014$. Therefore, most of the compression is mediated by a severe distortion of the Mn-O bonds of $\sim -2.7\%$.

The influence of strain on the bandwidth, W, of ABO_3 perovskite compounds is mediated through the relative modifications induced in the ⟨Mn-O-Mn⟩ bond angle and the Mn-O bond length, which control the overlap integrals between the Mn $3d$ and the O $2p$ orbitals [see Fig. 4(e)]. This double dependence is described by the empirical formula [19],

$$W \propto \frac{\cos\varphi}{d_{\mathrm{Mn\text{-}O}}^{3.5}}, \qquad (2)$$

$$\varphi = \frac{1}{2}(\pi - \langle\mathrm{Mn\text{-}O\text{-}Mn}\rangle) = \frac{2\alpha}{\sqrt{2}}, \qquad (3)$$

where φ is the "tilt" angle. In the bulk LSMO structure, ⟨Mn-O-Mn⟩ = 165.24° ($\varphi = 7.38°$, $\alpha = 5.2°$) and $d_{\mathrm{Mn\text{-}O}} = 1.964$ Å [37]. Thus combining Eqs. (2) and (3) one obtains $\frac{\cos\varphi}{d_{\mathrm{Mn\text{-}O}}^{3.5}} = 0.0934$. In the TW, the calculated value $\alpha_{\mathrm{TW}} = 7.5°$ corresponds to $\varphi_{\mathrm{TW}} = 10.68°$ (the ⟨Mn-O-Mn⟩ bond angle is decreased down to 158.64°). The distortion of the octahedral framework in the TW is thus described by $\delta\Theta/\Theta = -0.040$ and $\delta d/d = -0.027$, yielding $\frac{\cos\varphi}{d_{\mathrm{Mn\text{-}O}}^{3.5}} = 0.1019$. Therefore, despite the stronger angular distortion, the balance between $\delta\Theta/\Theta$ and $\delta d/d$ results in a broadening of the bandwidth inside the TW, thus explaining the observed enhancement in conductivity. It is worth mentioning that even smaller variations of the $\frac{\cos\varphi}{d_{\mathrm{Mn\text{-}O}}^{3.5}}$ ratio, induced in bulk manganites by cationic substitutions at the A site, cause huge variations in T_C of about 200 K [20]. This behavior is fully consistent with theoretical work showing that compressive strains in half-doped manganite epitaxial films promote an increase of T_C [21], in agreement with experimental observations at other doping levels such as for instance in $La_{0.8}Ba_{0.2}MnO_3$ [38]. With this in mind, the observed room temperature enhancement of the magnetic moment in the TWs can be explained as an apparent effect resulting from the strengthening of the magnetic interactions and, therefore, an increase in T_C.

IV. CONCLUSION

We have used a combination of electron microscopy, EELS, C-SFM, and MFM and modeling of the strained state of (100)-TWs in LSMO thin films that converge in signaling an enhancement of the electric conductivity and the strengthening of the magnetic interactions at TWs associated with a severe compression of the TW material. Notably, we find that the TWs are not affected by any significant chemical modification, and therefore the causes of their distinctive functional behavior are governed by geometrical effects that propitiate bandwidth broadening.

ACKNOWLEDGMENTS

We thank Julien Nicolaï for assistance with the I2TEM electron microscope in Toulouse (France). This research was sponsored by the Spanish MINECO (Grants No. MAT2011-29081-C02, No. MAT2012-33207, and No. MAT2013-47869-C4-1-P) projects. We also acknowledge financial aid from the Generalitat de Catalunya (2014 SGR 501). N.B. and F.S. also acknowledge funding from the European Union Seventh Framework Programme under Grant Agreement No. 312483-ESTEEM2 (Integrated Infrastructure Initiative I3) for providing access to aberration corrected electron microscopes at CEMES (Toulouse) and LPS (Orsay). R.G. and N.B. thank the Spanish MINECO for financial support through the FPI program. F.S. acknowledges support from the Labex (Excellence Laboratory) NEXT through a visiting scientist fellowship at CEMES (Toulouse, France).

[1] G. Catalan, J. Seidel, R. Ramesh, and J. F. Scott, Rev. Mod. Phys. **84**, 119 (2012).

[2] J. Seidel, G. Singh-Bhalla, Q. He, S.-Y. Yang, Y.-H. Chu, and R. Ramesh, Phase Transit. **86**, 53 (2013).

[3] P. Zubko, S. Gariglio, M. Gabay, Ph. Ghosez, and J. J.-M. Triscone, Annu. Rev. Condens. Matter Phys. **2**, 141 (2011).
[4] H. Y. Hwang, Y. Iwasa, M. Kawasaki, B. Keimer, N. Nagaosa, and Y. Tokura, Nat. Mater. **11**, 103 (2012).
[5] Y. Tokura, Phys. Today **56**, 50 (2003).
[6] J. Seidel, L. W. Martin, Q. He, Q. Zhan, Y.-H. Chu, A. Rother, M. E. Hawkridge, P. Maksymovych, P. Yu, M. Gajek, N. Balke, S. V. Kalinin, S. Gemming, F. Wang, G. Catalan, J. F. Scott, N. A. Spaldin, J. Orenstein, and R. Ramesh, Nat. Mater. **8**, 229 (2009).
[7] S. Farokhipoor and B. Noheda, Phys. Rev. Lett. **107**, 127601 (2011).
[8] T. Choi, Y. Horibe, H. T. Yi, Y. J. Choi, W. Wu, and S.-W. Cheong, Nat. Mater. **9**, 253 (2010).
[9] S. Farokhipoor, C. Magén, S. Venkatesan, J. Íñiguez, C. J. M. Daumont, D. Rubí, E. Snoeck, M. Mostovoy, C. de Graaf, A. Müller, M. Döblinger, C. Scheu, and B. Noheda, Nature (London) **515**, 379 (2014).
[10] T. Sluka, A. K. Tagantsev, P. Bednyakov, and N. Setter, Nat. Commun. **4**, 1808 (2013).
[11] P. Zubko, G. Catalan, A. Buckley, P. R. L. Welche, and J. F. Scott, Phys. Rev. Lett. **99**, 167601 (2007).
[12] A. Aird and E. K. H. Salje, J. Phys.: Condens. Matter **10**, L377 (1998).
[13] S. Van Aert, S. Turner, R. Delville, D. Schryvers, G. Van Tendeloo, and E. K. H. Salje, Adv. Mater. **24**, 523 (2012).
[14] J. Salafranca, R. Yu, and E. Dagotto, Phys. Rev. B **81**, 245122 (2010).
[15] J. Sapriel, Phys. Rev. **12**, 5128 (1975).
[16] C. W. Haas and W. F. Jaep, Phys. Lett. A **49**, 77 (1974).
[17] A. Borisevich, O. S. Ovchinnikov, H. J. Chang, M. P. Oxley, P. Yu, J. Seidel, E. A. Eliseev, A. N. Morozovska, R. Ramesh, S. J. Pennycook, and S. V. Kalinin, ACS Nano **4**, 6071 (2010).
[18] C. L. Jia, S.-B. Mi, K. Urbam, I. Vrejoiu, M. Alexe, and D. Hesse, Nat. Mater. **7**, 57 (2008).
[19] M. Medarde, J. Mesot, P. Lacorre, S. Rosenkranz, P. Fischer, and K. Gobrecht, Phys. Rev. B **52**, 9248 (1995).
[20] P. G. Radaelli, G. Iannone, M. Marezio, H. Y. Hwang, S.-W. Cheong, J. D. Jorgensen, and D. N. Argyriou, Phys. Rev. B **56**, 8265 (1997).
[21] A. Mukherjee, W. S. Cole, P. Woodward, M. Randeria, and N. Trivedi, Phys. Rev. Lett. **110**, 157201 (2013).
[22] A. Urushibara, Y. Moritomo, T. Arima, A. Asamitsu, G. Kido, and Y. Tokura, Phys. Rev. B **51**, 14103 (1995).
[23] N. M. Nemes, M. J. Calderón, J. I. Beltrán, F. Y. Bruno, F. García-Barriocanal, Z. Sefrioui, C. León, M. García-Hernández, M. C. Muñoz, L. Brey, and J. Santamaría, Adv. Mater. **26**, 7516 (2014).
[24] Z. Konstantinovic, J. Santiso, D. Colson, A. Forget, Ll. Balcells, and B. Martínez, J. Appl. Phys. **105**, 063919 (2009).
[25] F. Sandiumenge, J. Santiso, Ll. Balcells, Z. Konstantinovic, J. Roqueta, A. Pomar, J. P. Espinós, and B. Martínez, Phys. Rev. Lett. **110**, 107206 (2013).
[26] J. Santiso, Ll. Balcells, Z. Konstantinovic, J. Roqueta, P. Ferrer, A. Pomar, B. Martinez, and F. Sandiumenge, CrystEngComm. **15**, 3908 (2013).
[27] K. Yamanaka and S. Nakano, Appl. Phys. A **66**, S313 (1998).
[28] U. Rabe, E. Kester and W. Arnold, Surf. Interface Anal. **27**, 386 (1999).
[29] A. Gannepalli, D. G. Yablon, A. H. Tsou and R. Proksch, Nanotechnology **22**, 355705 (2011).
[30] F. de la Peña, M.-H. Berger, J.-F. Hochepied, F. Dynys, O. Stephan, and M. Walls, Ultramicroscopy, **111**, 169 (2011).
[31] P. Rez, Ultramicroscopy **28**, 16 (1989).
[32] See Supplemental Material at http://link.aps.org/supplemental/10.1103/PhysRevB.92.075111 for results on FMM and EELS.
[33] L. Peña, L. Garzón, R. Galceran, A. Pomar, B. Bozzo, Z. Konstantinovic, F. Sandiumenge, Ll. Balcells, C. Ocal, and B. Martínez, J. Phys.: Condens. Matter **26**, 395010 (2014).
[34] S. J. Pennycook and D. E. Jesson, Phys. Rev. Lett. **64**, 938 (1990).
[35] M. J. Hÿtch, Microsc. Microanal. Microstruct. **8**, 41 (1997).
[36] H. D. Megaw and C. N. W. Darlington, Acta Crystallogr. A **31**, 161 (1975).
[37] J. F. Mitchell, D. N. Argyriou, C. D. Potter, D. G. Hinks, J. D. Jorgensen, and S. D. Bader, Phys. Rev. B **54**, 6172 (1996).
[38] H. Chou, M.-H. Tsai, F. P. Yuan, S. K. Hsu, C. B. Wu, J. Y. Lin, C. I. Tsai, and Y.-H Tang, Appl. Phys. Lett. **89**, 082511 (2006).